Droplet collapse during strongly supercooled transitions

Daniel Cutting,[*] Essi Vilhonen,[†] and David J. Weir[‡]
Department of Physics and Helsinki Institute of Physics, P.O. Box 64, FI-00014 University of Helsinki, Finland

(Received 14 April 2022; accepted 25 October 2022; published 23 November 2022)

We simulate the decay of isolated, spherically symmetric droplets in a cosmological phase transition. It has long been posited that such heated droplets of the metastable state could form, and they have recently been observed in 3D multibubble simulations. In those simulations, the droplets were associated with a reduction in the wall velocity and a decrease in the kinetic energy of the fluid, with a consequent suppression in the gravitational wave power spectrum. In the present work, we track the wall speed and kinetic energy production in isolated droplets and compare them to those found in multibubble collisions. The late-time wall velocities that we observe match those of the 3D simulations, though we find that the spherical simulations are a poor predictor of the kinetic energy production. This implies that spherically symmetric simulations could be used to refine baryogenesis predictions due to the formation of droplets, but not to estimate any accompanying suppression of the gravitational wave signal.

DOI: 10.1103/PhysRevD.106.103524

I. INTRODUCTION

Many well-motivated extensions to the Standard Model have one or more cosmological phase transitions as a feature (see e.g. [1,2] and references therein). If such a phase transition is of first order, it can have interesting phenomenological consequences, such as the production of a baryon asymmetry [3], the generation of gravitational waves [4,5], or the seeding of intergalactic magnetic fields [6,7].

With upcoming gravitational wave detectors like LISA offering enhanced observational prospects for cosmological gravitational wave backgrounds, there have been increased efforts to understand first-order phase transitions in precise detail. Recent years have seen advances in the determination of the asymptotic wall speed for expanding bubbles [8–16], more precise calculations of the thermodynamic phase transition parameters and nucleation rates [17–26], and refined baryogenesis computations [27–31]. Holographic techniques have been used to compute phase transition parameters and gravitational wave signals [12,16,32–35]. Preliminary studies have explored the ability of LISA to reconstruct phase transition parameters [36,37]. New simulation techniques [38], valid for weak and intermediate thermal transitions, have enabled the exploration of the effects of density perturbations on the gravitational wave spectrum [39]. The first simulations of gravitational wave production from (magneto)hydrodynamic turbulence (including acoustic turbulence) have been conducted [40–45], and the gravitational wave signal from both strong thermal phase transitions [46,47] and vacuum-like transitions is being explored [48–53].

In Ref. [46], hot droplets of the metastable state were observed to form for strong transitions. This only occurred when the reaction front was a deflagration, in which the fluid is accelerated and heated ahead of the phase boundary. These hot droplets consist of relatively small regions of the metastable state (false vacuum) that are heated to well above the nucleation temperature, with the resulting pressure opposing the progress of the phase boundary.

The formation of droplets in a cosmological transition is not a new idea, and has been studied previously, primarily in the context of a QCD-like phase transition. Early works on cosmological phase transitions posited that, in the small-supercooling limit, transitions that proceeded via deflagrations would reheat a substantial fraction of the universe up to the critical temperature [54–61]. If such reheating were to take place, the growth of the bubbles would slow, and the final stages of the transition would involve the contraction of hot droplets of the metastable state. It was also argued that baryons could become trapped inside these shrinking droplets, leaving behind a baryon inhomogeneity on evaporation, or even resulting in persistent so-called "nuggets" of the metastable state. If axions are present during the transition, this can modify the stability of quark nuggets, leading to axion quark nuggets [62–65]. Furthermore, it has been suggested that this mechanism could have taken place in a dark sector [66], offering another scenario in which nuggets could comprise dark matter.

Other early works investigated the decay of spherical droplets using spherically symmetric simulations and found

[*]daniel.cutting@helsinki.fi
[†]essi.vilhonen@helsinki.fi
[‡]david.weir@helsinki.fi

that the fluid evolution exhibited self-similar behavior [67–69]. Spherical simulations of expanding bubbles in the small-supercooling limit with reflective boundary conditions were studied in Ref. [70]. The reflective boundary was intended to model the effect of interactions with "neighboring bubbles." When the compression wave from deflagrations collided with the boundary, it was found that the metastable region was reheated to the critical temperature at which the two phases become degenerate. As it cooled, the remaining metastable region subsequently collapsed with a substantially slower wall velocity than before.

In light of the above, the novelty of Ref. [46] was that droplets were observed in three-dimensional (3D) simulations with multiple bubbles, and away from the small-supercooling limit. Furthermore, it was seen that they were associated with a reduction in the expected kinetic energy fraction, which resulted in a suppression of the gravitational wave signal. The exact physical mechanism of this relationship was unclear.

In this paper, we revisit the formation and decay of droplets in the case of spherical symmetry. We focus on transitions with an expanding-bubble asymptotic wall speed of $\xi_w = 0.24$, as the droplets formed in these cases were the longest lasting in Ref. [46]. We perform a series of simulations of collapsing droplets with a range of transition strengths, moving away from the small-supercooling limit considered in earlier works. We track the wall velocity and measure the kinetic energy production of the droplets, comparing it to the multibubble results found in Ref. [46].

The layout of the paper is as follows. In Sec. II, we review the coupled field–fluid model used to model the phase transition. In Sec. III, we discuss the dynamics of expanding bubbles and shrinking droplets in first-order phase transitions, including similarity solutions and kinetic energy production. We describe our simulation code and the initial conditions in Sec. IV. We analyze the wall velocity and kinetic energy production of our simulations in Sec. V, and discuss similarity solutions in the context of our results. We conclude in Sec. VI. In the appendices, we provide a short description of the wall speed estimators used in this paper in Appendix A, then investigate the effect of varying the fractional change in the number of degrees of freedom and initial droplet radius in Appendices B and C, respectively.

II. COUPLED FIELD–FLUID MODEL

Hydrodynamical simulations of phase transitions often employ the coupled field–fluid model, in which a real scalar field is coupled to a perfect fluid via a dissipative friction term [60,71].

The energy–momentum tensor of the coupled field–fluid model is given by

$$T^{\mu\nu} = (\epsilon + p)U^\mu U^\nu + p g^{\mu\nu} + \partial^\mu\phi\partial^\nu\phi - \frac{1}{2}g^{\mu\nu}\partial_\rho\phi\partial^\rho\phi, \quad (1)$$

where ϵ and p are the internal energy density and pressure of the fluid, ϕ is the order parameter of the transition, and $U = \gamma(1, \mathbf{v})$ with $\mathbf{v}$ the fluid 3-velocity and γ the associated Lorentz factor. The enthalpy of the system is $w = \epsilon + p$.

The energy-momentum tensor can be split nonuniquely into a field and fluid piece, such that $T^{\mu\nu} = T^{\mu\nu}_\phi + T^{\mu\nu}_f$. We make the choice that

$$T^{\mu\nu}_f = (\epsilon + p)U^\mu U^\nu + g^{\mu\nu}p + Vg^{\mu\nu}, \quad (2)$$

$$T^{\mu\nu}_\phi = \partial^\mu\phi\partial^\nu\phi - g^{\mu\nu}(\partial\phi)^2 - Vg^{\mu\nu}, \quad (3)$$

where V is the effective thermal potential. We then assume that the interaction between the field and the fluid can be modelled via a phenomenological friction term

$$\partial_\mu T^{\mu\nu}_\phi = -\partial_\mu T^{\mu\nu}_f = \eta U^\mu\partial_\mu\phi\partial^\nu\phi, \quad (4)$$

where η is some constant friction parameter that is then set by the particle physics theory in question. In principle, η can be derived from the microphysics of the phase transition and may depend upon the order parameter and thermodynamic quantities in the vicinity of the bubble wall (or, more generally, the phase boundary) [11,14,72–74]. However, in this study we consider a simplified model in which we treat η as a constant free parameter.

An equation of state is needed to complete the field–fluid system. Following Ref. [46], we use a baglike equation of state:

$$\epsilon(T, \phi) = 3a(\phi)T^4 + V_0(\phi), \quad (5)$$

$$p(T, \phi) = a(\phi)T^4 - V_0(\phi), \quad (6)$$

where the zero-temperature effective potential is given by

$$V_0(\phi) = \frac{1}{2}M^2\phi^2 + \frac{1}{3}\mu\phi^3 + \frac{1}{4}\lambda\phi^4 - V_c. \quad (7)$$

Here V_c is a constant chosen such that the zero-temperature potential is normalized to $V_0(\phi_b) = 0$, where ϕ_b is the value of the scalar field in the broken phase. We denote the potential energy difference at zero temperature with $\Delta V_0 = V_0(0) - V_0(\phi_b)$. This choice of equation of state and effective potential is made for consistency with Ref. [46], where these droplets were first observed in a three-dimensional simulation.

The temperature-dependent potential in this model is then given by

$$V(\phi, T) = V_0(\phi) - T^4(a(\phi) - a_0), \quad (8)$$

where $a_0 = (\pi^2/90)g_*$ and g_* is number of the effective degrees of freedom in the symmetric phase.

The function $a(\phi)$ models the change in the effective degrees of freedom during the transition. We choose the form

$$a(\phi) = a_0 - \frac{\Delta V_0}{T_c^4}\left[3\left(\frac{\phi}{\phi_b}\right)^2 - 2\left(\frac{\phi}{\phi_b}\right)^3\right]. \quad (9)$$

This form is convenient as it ensures that the minima of V_0 at $\phi = 0$ and $\phi = \phi_b$ remain the minima of V for all temperatures T. The change in effective degrees of freedom is given by[1]

$$\Delta a \equiv a_0 - a(\phi_b) = \frac{\Delta V_0}{T_c^4}. \quad (10)$$

Furthermore, the two minima of the potential become degenerate at $T = T_c$, which is referred to as the critical temperature. Note that with our equation of state, the speed of sound

$$c_s = \sqrt{\frac{dp}{d\epsilon}} \quad (11)$$

is simply that of a relativistic fluid, $c_s^2 = 1/3$, in both phases. Although convenient, these choices represent a significant simplification. This simplification was made in previous work to ensure numerical stability when exploring systems with large supercooling. We defer exploration of more realistic effective potentials and equations of state to future work.

To describe the phase transition, we define a phase transition strength which measures the relative energy released during the transition with respect to the radiation energy already in the plasma,

$$\alpha = \frac{\theta(0, T_n) - \theta(\phi_b, T_n)}{\epsilon_r(T_n)}. \quad (12)$$

Here T_n is the nucleation temperature and $\epsilon_r = 3w/4$ is the radiation energy density in the symmetric phase, in this case $\epsilon_r = 3a_0 T_n^4$. The trace anomaly θ is given by

$$\theta(\phi, T) = \frac{1}{4}(\epsilon(\phi, T) - 3p(\phi, T)). \quad (13)$$

Assuming spherical symmetry, we can derive the equation of motion for the scalar field by considering $\partial_\mu T^{\mu\nu}_\phi$:

$$-\ddot{\phi} + \frac{1}{r^2}\partial_r(r^2\partial_r\phi) - \frac{\partial V}{\partial\phi} = \eta\gamma(\dot{\phi} + v\partial_r\phi). \quad (14)$$

Here v is positive when the fluid velocity is pointed radially outward. Equations of motion for our other dynamical variables, the fluid energy density $E = \gamma\epsilon$ and the fluid momentum density $Z = \gamma^2 wv$, can be derived from $\partial_\mu T^{\mu\nu}_f$:

$$\dot{E} + \frac{1}{r^2}\partial_r(r^2 E v) + p\left[\dot{\gamma} + \frac{1}{r^2}\partial_r(r^2\gamma v)\right] - \frac{\partial V}{\partial\phi}\gamma(\dot{\phi} + v\partial_r\phi) = \eta\gamma^2(\dot{\phi} + v\partial_r\phi)^2, \quad (15)$$

$$\dot{Z} + \frac{1}{r^2}\partial_r(r^2 Z v) + \partial_r p + \frac{\partial V}{\partial\phi}\partial_r\phi = -\eta\gamma(\dot{\phi} + v\partial_r\phi)\partial_r\phi. \quad (16)$$

In both cases we have taken the friction term of Eq. (4) into account. These equations can then be discretized and solved numerically, see Sec. IV.

III. HYDRODYNAMICS OF EXPANDING BUBBLES AND SHRINKING DROPLETS

In a thermal first-order phase transition, bubbles of the true vacuum nucleate in the presence of a cosmic plasma. As the bubbles expand, the friction between the bubble wall and plasma causes a heated fluid shell to develop. After sufficient time, the fluid profile reaches an asymptotic form.

The asymptotic fluid profile takes a qualitatively different form depending on the expanding-bubble asymptotic wall speed ξ_w.[2] If the wall speed is subsonic, the transition front propagates as a deflagration. In a deflagration, the fluid is accelerated and heated at a leading-edge shock front. The fluid reaches its peak velocity at the transition boundary. When the fluid crosses the transition boundary, it decelerates and ends up at rest inside the bubble.

Walls travelling faster than the Jouguet detonation speed c_J give rise to a detonation. The Jouguet detonation speed is dependent on the transition strength, but it is always larger than the speed of sound. In such a transition, the bubble wall hits fluid that is at rest. The fluid is then heated and accelerated as it crosses the transition boundary, before decelerating inside the bubble.

In deflagrations, the heated fluid precedes the advancing bubble wall. In sufficiently strong phase transitions, when the heated fluid shells of multiple bubbles meet, the temperature of the metastable state can become substantially higher than the nucleation temperature. This effect has been noted recently in hydrodynamical simulations of multiple bubbles colliding in 3D, see Ref. [46]. In that paper, it was found that these heated regions of the metastable state could persist for long periods of time, effectively extending the duration of the phase transition and reducing the wall velocity. These long-lasting regions

[1]Note in some references a_0, the degrees of freedom in the symmetric phase, is denoted a_+. Similarly $a(\phi_b)$ is sometimes written as a_-.

[2]Note that we distinguish between the asymptotic wall speed ξ_w reached at late times for isolated expanding bubbles, and the wall velocity v_w measured or observed at a given time.

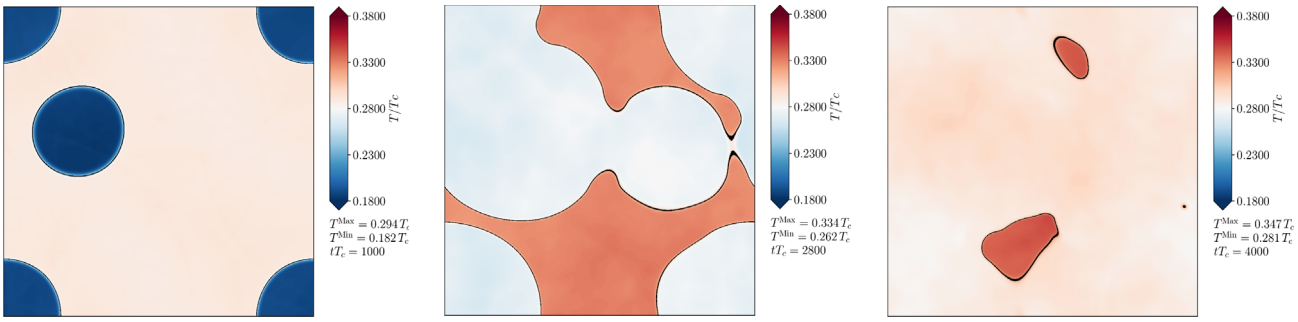

(a) Early (b) Intermediate (c) Late

FIG. 1. 2D slices of the temperature during a 3D simulation from Ref. [46], showing eight bubbles expanding with an asymptotic expanding-bubble wall speed $\xi_{\rm w} = 0.24$ and a transition strength $\alpha = 0.34$. The simulation had periodic boundary conditions and one of the bubbles was nucleated in the corners of the slice. The nucleation temperature was $T_{\rm n} = 0.28T_{\rm c}$. Black lines are used to highlight the phase transition boundary.

were referred to as *droplets* of the metastable state, as these have been discussed previously in the literature, in particular in reference to the QCD phase transition [56,67,68]. It should be noted that droplets cannot form for detonations as the fluid is at rest ahead of the bubble wall.

In Fig. 1, we show an example of the evolution of the temperature for a deflagration (the results of this simulation were previously presented in Ref. [46]). Three snapshots of the temperature are shown, taking 2D slices through the 3D simulation, first early on in the phase transition while the bubbles remain isolated, then at an intermediate time where the heated fluid shells have collided, and finally at a late time where only heated droplets of the metastable state remain. In the simulation shown, η was chosen such that the asymptotic expanding-bubble wall speed of isolated bubbles was $\xi_{\rm w} = 0.24$, and the transition strength was $\alpha = 0.34$. As can be seen, once the fluid shells collide, the phase boundary begins to deform. A clear temperature difference is seen between the metastable and true vacuum regions. At late times only small droplets of the metastable state persist.

The results of Ref. [46] indicated that the walls slowed down as the transition approached completion, and that the effect was more pronounced for stronger transitions. To illustrate how the wall speed slows as droplets form, we have taken simulations from Ref. [46] with the same asymptotic expanding-bubble wall speed $\xi_{\rm w} = 0.24$ and a variety of transition strengths α. For each simulation, we plot the evolution of the wall speed $v_{\rm w}$ as a function of time in Fig. 2. As can be seen, initially the walls accelerate toward $\xi_{\rm w}$, but at some point the fluid shells begin to collide and thus heat up the metastable state. At the same time the phase boundaries start to decelerate. The stronger the phase transition, the more the metastable state is heated above the nucleation temperature, and the more the phase boundary decelerates.

The formation of droplets was associated with a decrease in the kinetic energy production and substantial suppression of the gravitational wave signal. The deceleration of the phase boundary could also have an effect on baryogenesis, as it has been shown that the efficiency of generating a baryon asymmetry has a strong wall velocity dependence (see e.g. Refs. [30,75]).

A. Similarity solutions

When the phase boundary of a droplet or a bubble reaches a terminal wall velocity, the fluid profile approaches an asymptotic shape. To find the form that this asymptotic profile takes, we need to match the fluid velocity and enthalpy across the phase boundary.

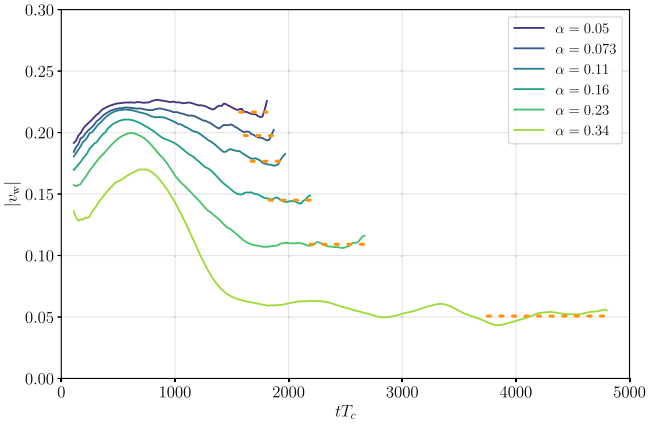

FIG. 2. Wall speed in 3D simulations from Ref. [46] of colliding bubbles with asymptotic expanding-bubble wall speeds of $\xi_{\rm w} = 0.24$. The different colors correspond to simulations with different transition strengths. The lines end when the metastable state takes up less than 2% of the total volume. A late-time wall speed for each simulation is shown with an orange dashed line. The line extends over the times for which $|v_{\rm w}|$ is fitted, corresponding to when the broken phase takes up between 10% and 2% of the total volume. See Table IV for the late-time values of $|v_{\rm w}|$. See Appendix A for a discussion of wall speed estimators.

Taking the energy-momentum tensor for a perfect fluid,

$$T^{\mu\nu} = (\epsilon + p)U^\mu U^\nu + g^{\mu\nu} p, \tag{17}$$

with enthalpy $w = \epsilon + p$, the conservation of energy and momentum density across the phase boundary leads to

$$w_+ \tilde{\gamma}_+^2 \tilde{v}_+^2 + p_+ = w_- \tilde{\gamma}_-^2 \tilde{v}_-^2 + p_-, \tag{18}$$

$$w_+ \tilde{\gamma}_+^2 \tilde{v}_+^2 = w_- \tilde{\gamma}_-^2 \tilde{v}_-^2, \tag{19}$$

where $\tilde{v}$ and $\tilde{\gamma}$ refer to the fluid velocity and the corresponding Lorentz factor in a frame moving along with the phase boundary. Subscripts $+$ and $-$ refer to the quantities just ahead and just behind the wall, respectively.

Once the velocity and enthalpy have been obtained on both sides of the phase boundary, it is possible to find a solution for the rest of the fluid profile by considering the continuity equation,

$$\partial_\nu T^{\mu\nu} = 0. \tag{20}$$

Imposing spherical symmetry, it is possible to find differential equations for w and v in terms of a self-similarity variable constructed from a combination of a radial and time coordinate, $\xi = r/\mathcal{T}$ [76,77]. These differential equations can be written in the following parametric form, see e.g. Refs. [78,79]:

$$\frac{\mathrm{d}\xi}{\mathrm{d}\tau} = \xi[(\xi - v)^2 - c_\mathrm{s}^2(1 - \xi v)^2], \tag{21}$$

$$\frac{\mathrm{d}v}{\mathrm{d}\tau} = 2vc_\mathrm{s}^2(1 - v^2)(1 - \xi v), \tag{22}$$

$$\frac{\mathrm{d}w}{\mathrm{d}\tau} = w\left(1 + \frac{1}{c_\mathrm{s}^2}\right)\gamma^2 \mu \frac{\mathrm{d}v}{\mathrm{d}\tau}, \tag{23}$$

where

$$\mu(\xi, v) = \frac{\xi - v}{1 - \xi v} \tag{24}$$

is the fluid velocity at ξ in a frame moving with velocity ξ.

Solving these differential equations gives us a set of similarity-profile curves, with the solutions for the velocity profiles shown in Fig. 3. Values of $\xi > 0$ correspond to expanding bubbles. In this case, $\mathcal{T}$ is the time since the nucleation of the bubble, and r the distance from the bubble centre. On the other hand, profiles with $\xi < 0$ correspond to shrinking droplets. Then, r is the distance from the droplet center, and $\mathcal{T}T_\mathrm{c} = 0$ corresponds to the time at which the droplet evaporates, with the droplet radius $R_\mathrm{d} \to +\infty$ when $\mathcal{T} \to -\infty$. From the plots, it can be seen that the velocity curves have fixed points for τ at $(\xi, v) = (\pm c_\mathrm{s}, 0)$. For an indicative sketch of the droplet case, see Fig. 4.

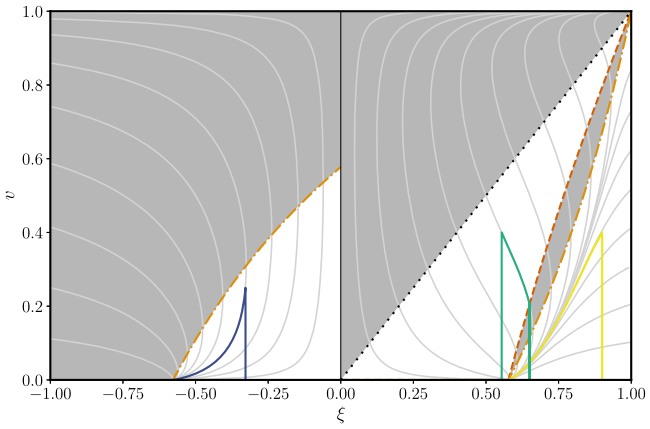

FIG. 3. Similarity curves for the fluid velocity profiles obtained from solving Eqs. (21) and (22). Positive values of ξ correspond to bubbles and negative values to droplets. The similarity curves are shown in light gray, and the solid-colored lines show example profiles, from left to right, for a droplet, a deflagration and a detonation. The two orange dash-dotted lines indicate the sound speed in a frame moving at velocity ξ, the red dashed line indicates the velocity of a deflagration shock front, and the black dotted line indicates the maximum fluid velocity allowed for a bubble profile. Regions with unphysical velocity profiles are shaded dark gray. For a thorough treatment on similarity curves in a cosmological transition, see Chapter 11.1 in Ref. [80].

In order to construct the self-similar profile, a wall speed and a peak fluid velocity are chosen, which sets the initial point on the (ξ, v) plane. Using Eqs. (21) and (22), the velocity profile can be constructed by integrating backwards toward the fixed point at $(\xi, v) = (c_\mathrm{s}, 0)$. Also drawn on the plot are lines indicating the sound speed in a frame moving at velocity ξ, i.e. $v = \mu(\xi, \pm c_\mathrm{s})$. For bubbles, this

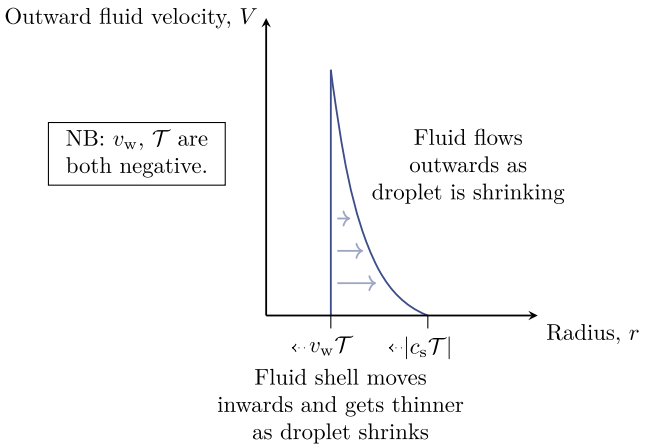

FIG. 4. Sketch of a droplet similarity solution in context. The fluid flows outwards as the phase boundary moves inwards (at speed $|v_\mathrm{w}|$). The wedge of fluid becomes thinner with time, as the outer boundary of the wedge also travels inwards (at speed c_s). However, the width of the wedge in terms of the parameter $\xi = r/\mathcal{T}$ remains constant.

sets the maximum fluid velocity for a detonation, whereas for droplets it separates the physical subsonic deflagration profiles from the unphysical sonic and supersonic deflagrations (i.e. droplets with $\xi_w \geq c_s$). For bubbles, the fluid velocity cannot exceed $v = \xi$, as in the wall frame this would mean that the fluid would be flowing outwards from inside the bubble. Finally, the speed at which the leading edge of a deflagration shock propagates is shown for bubbles. For deflagrations, when the velocity similarity curve hits this line, there is a discontinuity in the profile with $v = 0$ for larger values of ξ. Similar curves can be constructed for the enthalpy profiles.

B. Kinetic energy fraction and gravitational waves

An important quantity for the generation of gravitational waves is the kinetic energy fraction,

$$K = \frac{\langle w\gamma^2 v^2 \rangle}{\langle w\gamma^2 v^2 + e \rangle} \equiv \frac{\langle w\gamma^2 v^2 \rangle}{\langle e \rangle}, \tag{25}$$

namely, the volume-averaged kinetic energy relative to the volume-averaged total energy density $\langle e \rangle$ at the end of the transition. It has previously been shown that the amplitude of the gravitational wave power spectrum is proportional to K^2 [81,82]. Estimates of K that do not require expensive 3D numerical simulations are therefore highly desirable. The typical procedure is to find the asymptotic profile of a bubble expanding in isolation and to assume that the value of K extracted from the fluid profile matches well onto the final result obtained from many bubbles colliding in the 3D numerical simulation. While this procedure is known to be accurate for weak and intermediate-strength transitions [81,82], it breaks down for strong transitions where heated fluid shells start interacting with each other nonlinearly. In particular, heated droplets of the metastable state form in strong deflagrations, and in Ref. [46] it was proposed that the formation of these droplets was associated with a drop in K relative to that predicted from an isolated bubble.

In this work, we track the kinetic energy fraction in the fluid for spherically symmetric bubbles and droplets. We define the kinetic energy fraction of a bubble as

$$K_b(t) = \frac{\int_0^\infty \mathrm{d}r\, r^2 w\gamma^2 v^2}{\int_0^{R_b(t)} \mathrm{d}r\, r^2 e(t=0)}, \tag{26}$$

with $R_b(t)$ the bubble radius at time t after nucleation. The numerator is the kinetic energy of the fluid shell around the bubble. For the denominator, we consider the region converted into the true vacuum by the bubble at time t, and find the total energy of the system that was contained within that volume at $t = 0$. We sometimes use the notation $K_b(R_{ref})$, which indicates the value $K_b(t)$ at the time t for which the radius of the bubble is given by a reference radius, $R_b(t) = R_{ref}$. This is a unique time, as the bubble radius is monotonically increasing with respect to t for an isolated expanding bubble.

Similarly, we define the kinetic energy fraction for a droplet to be

$$K_d(t) = \frac{\int_0^\infty \mathrm{d}r\, r^2 w\gamma^2 v^2}{\int_{R_d(t)}^{R_{d0}} \mathrm{d}r\, r^2 e(t=0)}, \tag{27}$$

with R_{d0} the initial droplet radius. Analogous to the previous expression, for the denominator we consider the region converted into the true vacuum at time t and calculate the initial total energy of the system contained in that region. Note the different limits of integration when compared with Eq. (26).

Comparing these two quantities for a droplet released from R_{d0} and a bubble for which $R_b(t) = R_{d0}$ gives a measure of the relative efficiency of producing kinetic energy for droplets.

Another quantity that is often measured in simulations is the enthalpy-weighted mean square fluid 4-velocity

$$\bar{U}_f^2 = \frac{\langle w\gamma^2 v^2 \rangle}{\bar{w}}. \tag{28}$$

with $\bar{w}$ the mean enthalpy density. $\bar{U}_f^2$ is related to the kinetic energy faction via

$$K = \Gamma \bar{U}_f^2, \tag{29}$$

where

$$\Gamma = \frac{\bar{w}}{\bar{e}} \tag{30}$$

is the mean adiabatic index in the fluid.

While we could in principle also estimate $\bar{U}_f^2$ from our spherical simulations, in practice this leads to severe inconsistencies for strong transitions where w after the transition can differ significantly from its initial value. To illustrate this, let us define

$$\bar{U}_{f,b}^2(t) = \frac{\int_0^\infty \mathrm{d}r\, r^2 w\gamma^2 v^2}{\int_0^{R_b(t)} \mathrm{d}r\, r^2 w_n}, \tag{31}$$

for bubbles in line with previous three-dimensional simulation work.

The denominator for $K_b(t)$ in Eq. (26) is the initial total energy of the system for the volume converted into the true vacuum by a bubble at time t. For $\bar{U}_{f,b}^2(t)$ it is the initial enthalpy of the system for the equivalent volume. However, while the energy is conserved, the enthalpy is not. Therefore, while the denominator of Eq. (26) is an accurate estimate of the total energy density in Eq. (25), we cannot easily estimate the denominator of Eq. (28) for an isolated bubble or droplet.

IV. METHODS

In this study, we present results from evolving spherically symmetric bubbles and droplets in the coupled field–fluid model. Due to spherical symmetry, we are able to evolve the equations of motion of Eqs. (14)–(16) on a 1D lattice. To do this, we use a simplified 1D version of the SCOTTS code used in Refs. [46,81,82]. This is based on the 1D code of Ref. [60], which implements a Minkowski space version of the algorithms outlined in Refs. [83–85]. For the evolution of the scalar field, a Crank–Nicolson update [86] is used. For the hydrodynamical evolution, the code uses operator splitting to update each term in Eqs. (15) and (16) and upwind donor cell for the advection terms.

Our initial conditions in the spherical simulations depend on whether we are performing a simulation of a droplet or a bubble. For bubbles, we initially prepare the scalar field to be in the broken phase close to the origin and in the symmetric phase away from the centre of the bubble. We use a Gaussian profile

$$\phi(r) = \phi_{\rm b} \exp\left(\frac{-r^2}{2R_{\rm c}^2}\right) \tag{32}$$

with

$$R_{\rm c} = \frac{2\sigma}{V(0,T_{\rm n}) - V(\phi_{\rm b},T_{\rm n})}, \tag{33}$$

the critical radius in the thin-wall approximation. In the equation above, σ refers to the surface tension in the thin-wall approximation and is given by

$$\sigma = \frac{(\mu^2 + \mu\sqrt{\mu^2 - 4M^2\lambda} - 2M^2\lambda)^{3/2}}{24\lambda^{5/2}}. \tag{34}$$

For droplets, we instead prepare the field profile to be in the symmetric phase at the origin and in the broken phase far away from it. We choose an initial droplet radius, $R_{\rm d0}$, and then fix the wall profile using a tanh-shape. The scalar field is then set using

$$\phi(r) = \frac{\phi_{\rm b}}{2}\left(1 - \tanh\left(\frac{R_{\rm d0} - r}{l_{\rm w}}\right)\right), \tag{35}$$

with wall thickness $l_{\rm w}$ given by the thin-wall approximation,

$$l_{\rm w} = \frac{2}{\sqrt{V''(\phi_{\rm b},T_{\rm c})}}. \tag{36}$$

Note that, even for bubbles nucleated with a Gaussian or "thick-wall" profile like that in Eq. (32), we still expect the phase boundary to relax to a tanh-like profile as it expands. This is due to the phenomenological friction term of Eq. (4), and motivates the form of the initial droplet profile given above.

TABLE I. Table of key constant quantities for the computations in this paper. The input parameters are the effective degrees of freedom during the transition g_* and the potential parameters M^2, μ and λ. Using the potential parameters, the broken phase scalar field minimum $\phi_{\rm b}$, the change in degrees of freedom Δa during the transition, Eq. (10), and the reaction front (wall) thickness $l_{\rm w}$, Eq. (36), can be derived.

g_*	$M^2/T_{\rm c}^2$	$\mu/T_{\rm c}$	λ	$\phi_{\rm b}/T_{\rm c}$	$\Delta a/a_0$	$l_{\rm w}T_{\rm c}$
106.75	0.0427	0.168	0.0732	2.00	0.0059	5.23

In the initial conditions for both droplets and bubbles, we initialise the fluid such that $T = T_{\rm n}$ and $\mathbf{v} = 0$ everywhere. Note that this differs from other studies of the evolution of droplets, where the simulations are initialized with an initial temperature jump across the phase boundary [67–69]. In this work we are also interested in the heating caused by the collapse of the droplet and the effect this has on the phase boundary velocity and kinetic energy production. We hence leave simulations in which a temperature jump is initialized based on values extracted from droplets formed in 3D multibubble simulations for future work.

We match our potential parameters to those used in Ref. [46] for ease of comparison with earlier 3D multibubble simulations. The potential parameters and the corresponding wall thickness are given in Table I (see Appendix B for an investigation of varying the fractional change in the number of degrees of freedom).

We use a lattice spacing $\Delta x T_{\rm c} = 1.0$ in all the simulations. For our droplet simulations, we set the initial droplet radius $R_{\rm d0}T_{\rm c} = 2 \times 10^4$ (see Appendix C for an investigation of the consequences of varying the droplet radius). Other simulation parameters, such as the timestep Δt and the simulation duration $t_{\rm fin}$, are given for the 1D runs in Table II. We set the number of simulation sites $L = t_{\rm fin}/\Delta x$.

We perform simulations of bubbles which expand with an asymptotic wall speed $\xi_{\rm w} = 0.24$. In this model, the strength α is varied by varying $T_{\rm n}$, keeping all other input parameters constant. We pick a range of $T_{\rm n}$ that gives transitions spanning from $\alpha = 0.005$ up to $\alpha = 0.41$, which is close to the maximum α allowed[3] for $\xi_{\rm w} = 0.24$. For each value of $T_{\rm n}$, we find the value of η that gives $\xi_{\rm w} = 0.24$ for a bubble, and then also run an equivalent droplet simulation with this value of η. We list these values in Table II. We also perform comparisons with 3D multibubble simulations. These correspond to the simulations with $\xi_{\rm w} = 0.24$ in

[3]As discussed at the end of Sec. III A, the peak fluid velocity in a self-similar flow cannot exceed the wall velocity. As increasing α while keeping $\xi_{\rm w}$ fixed increases the peak fluid velocity, this implies there is a maximum value of α for a self-similar flow with a given $\xi_{\rm w}$.

TABLE II. Parameters used for the spherically symmetric 1D runs, split according to droplet [Eq. (35)] or bubble [Eq. (32)] initial condition type. For each transition strength α, we list the nucleation temperature T_n relative to the critical temperature T_c, the friction parameter η, the timestep Δt and the final time in the simulation t_{fin}. For the bubble runs we also list the critical radius R_c as given by Eq. (33).

Type	α	T_n/T_c	η/T_c	$\Delta t T_c$	$t_{fin}T_c$	R_cT_c
Droplet	0.0050	0.79	0.68	0.2	3.0×10^5	⋯
	0.050	0.45	1.2	0.2	3.0×10^5	⋯
	0.073	0.41	1.3	0.2	3.0×10^5	⋯
	0.11	0.37	1.5	0.2	3.0×10^5	⋯
	0.16	0.33	1.8	0.2	3.0×10^5	⋯
	0.23	0.30	2.4	0.2	3.0×10^5	⋯
	0.34	0.28	5.1	0.2	6.4×10^5	⋯
	0.41	0.26	11	0.1	6.4×10^5	⋯
Bubble	0.0050	0.79	0.68	0.2	0.9×10^5	12
	0.050	0.45	1.2	0.2	0.9×10^5	7.7
	0.073	0.41	1.3	0.2	0.9×10^5	7.6
	0.11	0.37	1.5	0.2	0.9×10^5	7.5
	0.16	0.33	1.8	0.2	0.9×10^5	7.5
	0.23	0.30	2.4	0.2	0.9×10^5	7.4
	0.34	0.28	5.1	0.2	0.9×10^5	7.4
	0.41	0.26	11	0.1	0.9×10^5	7.4

TABLE III. List of 3D multibubble simulations from Ref. [46] used for comparison in this paper. In addition to the parameters given above, all simulations had $L^3 = 960^3$ lattice sites, $N_b = 8$ bubbles, $\Delta x T_c = 1.0$, $\Delta t T_c = 0.2$ and final time $t_{fin}T_c = 4.8\times10^3$.

α	T_n/T_c	η/T_c	R_cT_c
0.050	0.45	1.2	7.7
0.073	0.41	1.3	7.6
0.11	0.37	1.5	7.5
0.16	0.33	1.8	7.5
0.23	0.30	2.4	7.4
0.34	0.28	5.1	7.4

Ref. [46], which we list again here in Table III for convenience.

V. RESULTS

In our spherical droplet simulations, the phase boundary is released from rest with initial bubble radius R_{d0} at the start of each simulation. The droplet starts shrinking. At the same time, an inward-moving fluid shell is generated in the interior of the droplet and travels toward the center of the droplet faster than the phase boundary itself. As this fluid shell propagates, the temperature rises and the phase boundary begins to slow. When the inward-moving fluid shell hits the origin, it rebounds, and a reflected fluid shell is driven back toward the phase boundary. When the reflected fluid shell meets the phase boundary, part of the fluid shell can once more be reflected toward the origin.[4] This process can happen several times before the droplet evaporates. The interaction of the fluid with the phase boundary can significantly decelerate the phase boundary, and for stronger transitions the droplet can even be forced to temporarily grow in size before shrinking again.

We show the evolution of the scalar field, velocity and temperature profiles for a droplet with a relatively weak transition strength $\alpha = 0.05$ in Fig. 5, and for one with a stronger transition strength $\alpha = 0.34$ in Fig. 6. The late-time evolution of the fluid profile in the simulation of $\alpha = 0.34$ demonstrates self-similarity once the interior of the droplet no longer contains any significant fluid perturbations. Movies of these simulations are available at Ref. [88].

We track the velocity v_w of the phase boundary in our spherical droplet simulations (see Appendix A). We plot the evolution of v_w for each simulation in the upper panel of Fig. 7. When v_w is negative, the droplet is shrinking, with the phase boundary moving toward the origin. For positive values of v_w, the phase boundary is moving outward, causing the droplet to temporarily increase in size. For the smallest transition strength, $\alpha = 0.005$, we see that the phase boundary travels toward the origin with speed close to that of an expanding bubble, with $v_w \approx -0.24$. At larger transition strengths, v_w rapidly decelerates as the phase boundary slows and the temperature immediately inside the droplet increases. For the strongest transitions it can be noticed that v_w becomes temporarily positive.

As we noted above, the fluid shells can be reflected between the origin and the phase boundary multiple times. While this is happening, the phase boundary velocity v_w oscillates with shrinking amplitude, before settling toward an asymptotic value. We can see that the late-time wall velocity tends toward zero as the transition strength increases. Furthermore, for the two strongest transitions, $\alpha = 0.34$ and $\alpha = 0.41$, we see that the final wall velocity is reached a long time before the droplet evaporates. Comparison with the late-time evolution of the profiles in Fig. 6 indicates that a self-similar profile is obtained before the evaporation of the droplet. We will discuss this in more detail in Sec. V A.

In Fig. 8, we compare the late-time wall velocities $v_{w,late}$ found in the spherical simulations with those extracted from the multibubble simulations of Ref. [46]. There is broad agreement across the range of α we consider, indicating that the late-time propagation of the phase boundary in a droplet can be well modelled from a spherical simulation. This seems independent of whether or not we

[4]Note that similar reflections of the fluid at phase boundaries can be seen in the movies of the temperature for the multibubble transitions in Ref. [46], which are available at Ref. [87].

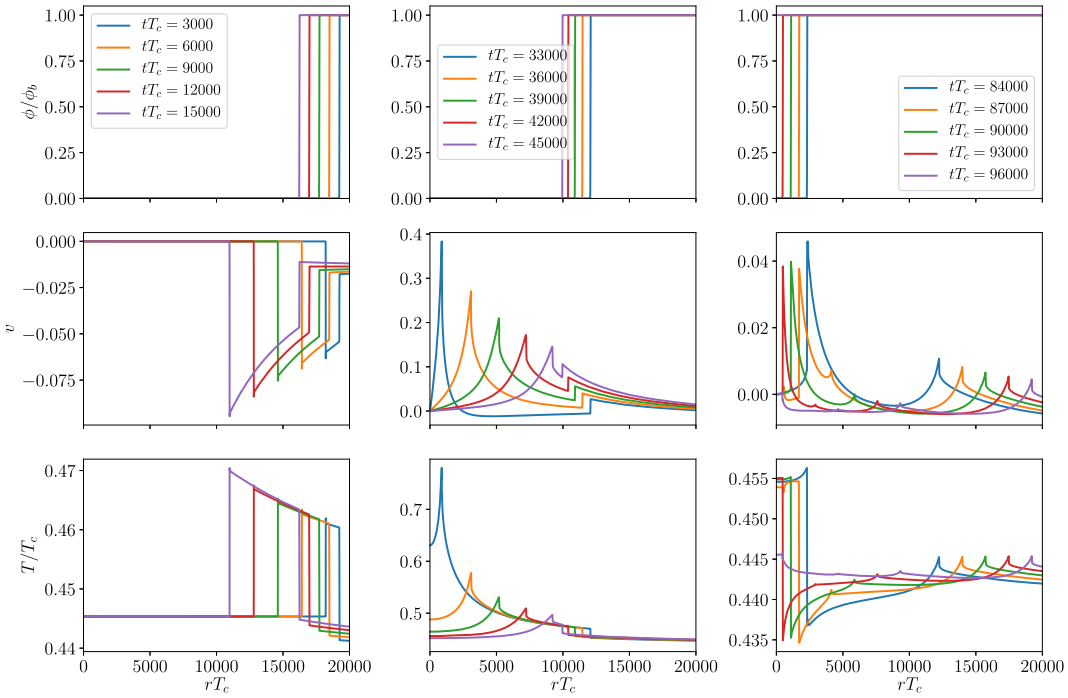

FIG. 5. Evolution of ϕ, v, and T for a spherical droplet simulation with $\alpha = 0.05$. The top panel in each row shows the profile of the scalar field at various times, the middle panel shows the profile of the fluid velocity, and the bottom panel shows the temperature. The left column shows the evolution at early times, when the fluid shell is beginning to develop. The middle column shows intermediate times, after the fluid shell has been reflected at the origin. The right column shows late times, shortly before the droplet evaporates. As we do not find a similarity solution for weak transitions before the droplet evaporates, the late-time behavior of the system appears less straightforward than for the strong transition seen below in Fig. 6. Note that the y-axis ranges change between columns for v and T. A movie of this simulation is available at Ref. [88].

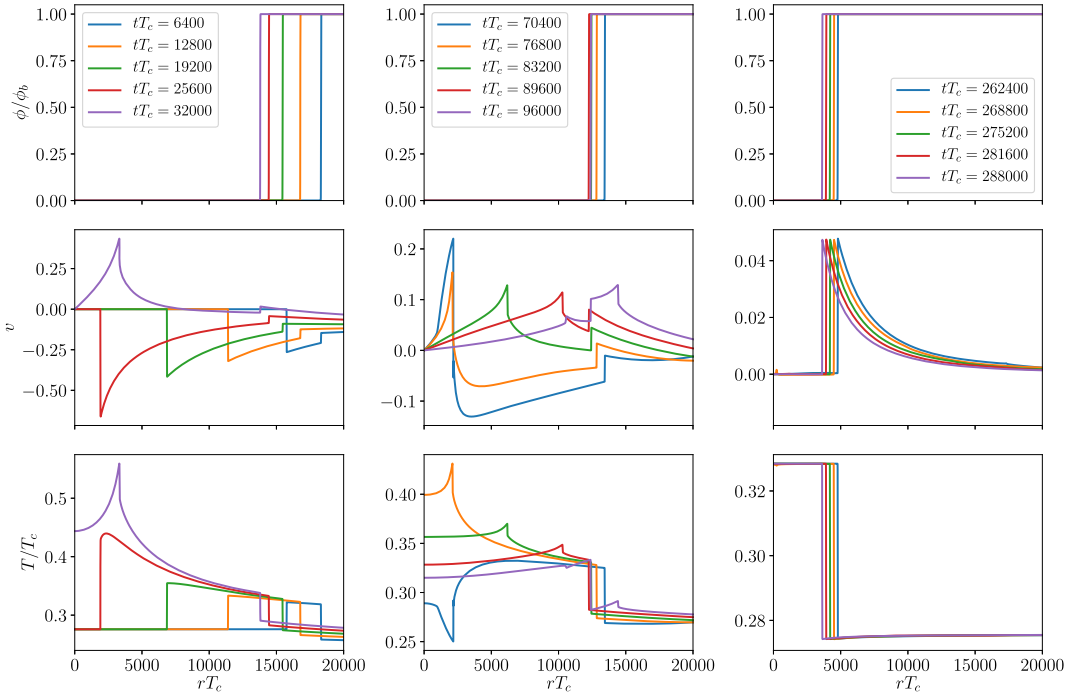

FIG. 6. Evolution of ϕ, v, and T for a spherical droplet simulation with $\alpha = 0.34$. As in Fig. 5, we show the situation at early, intermediate and late times. Note, however, that the exact times differ, as the droplet shrinks at a slower rate. Notably, the late-time behavior in this case is that of a similarity solution of the fluid equations. Again, the y-axis ranges change between columns for v and T. A movie of this simulation is available at Ref. [88].

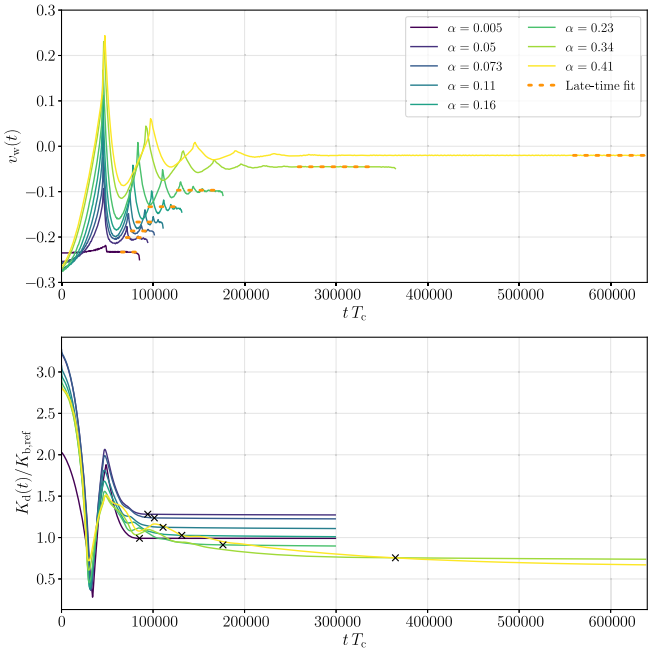

FIG. 7. In the top panel we show the evolution of the wall velocity in the spherical droplet simulations. See Appendix A for a discussion on wall speed estimators. Each solid line corresponds to an individual simulation with a given α. These lines end when the phase boundary reaches the origin. We average over v_w when $0.05R_{d0} < R_d < 0.25R_{d0}$ to find The values of $v_{w,late}$ and the times averaged over are shown with dashed orange lines. In the bottom panel we show the evolution of K_d in each simulation. We normalize K_d [see Eq. (27)] according to the value of $K_b(R_{ref})$ [see Eq. (26)] for a bubble with the same values of α and η and with radius $R_{ref} = R_{d0}$. The black crosses on the bottom panel refer to the time at which the phase boundary reaches the origin. Values of $v_{w,late}$ and of $K_d/K_b(R_{ref})$ at the black crosses are given in Table IV.

reach a similarity solution in the spherical droplet simulation.

Next, we look at the kinetic energy fraction K_d [see Eq. (27)] for droplets, noting that it is a key parameter for predicting gravitational wave power spectra. In the bottom panel of Fig. 7, we show the evolution of K_d in the aforementioned spherical droplet simulations. We normalise K_d by using $K_b(R_{ref})$ [see Eq. (26)], which is taken from a bubble with the same value of η and α at a given reference radius R_{ref}. In this case, we set $R_{ref} = R_{d0}$. This quantity then provides a measure of the relative efficiency for which a droplet system produces kinetic energy compared to an isolated, expanding bubble.

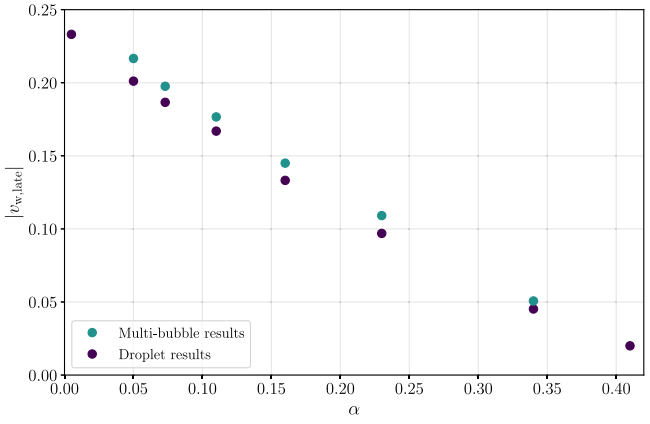

FIG. 8. Late-time wall speeds $|v_{w,late}|$ in both 3D multibubble simulations and spherical droplet simulations. Values are taken from Table IV, see the caption for details.

TABLE IV. Comparison of results from the spherically symmetric 1D droplet simulations and the 3D multibubble simulations of Ref. [46]. We show the late-time wall speed $|v_{w,late}|$ and the relative kinetic efficiency $K/K_b(R_{ref})$ for each transition strength. The value of $|v_{w,late}|$ is found from a fit to $|v_w|$ for $0.05R_{d0} < R_d < 0.25R_{d0}$ in the spherical droplet simulations, and for when the broken phase volume is between 10% and 2% in the multibubble simulations. See Appendix A for a discussion on wall speed estimators. The values of $K/K_b(R_{ref})$ refer to the value of K_d [see Eq. (27)] at droplet evaporation in the spherical simulations, see black crosses in Fig. 7, and to the peak value of K [see Eq. (25)] in the multibubble simulations. $K_b(R_{ref})$ [see Eq. (26)] corresponds to the kinetic energy of an isolated bubble with radius $R_{ref} = R_{d0}$ for the spherical droplets and with $R_{ref} = R_*/2$ for the multibubble simulations.

	$\lvert v_{w,late}\rvert$		$K/K_b(R_{ref})$	
α	Droplet	Multibubble	Droplet	Multibubble
0.0050	0.23	...	0.99	...
0.050	0.20	0.22	1.3	0.91
0.073	0.19	0.20	1.2	0.81
0.11	0.16	0.18	1.1	0.63
0.16	0.14	0.15	1.0	0.46
0.23	0.099	0.11	0.91	0.26
0.34	0.045	0.051	0.76	0.11
0.41	0.020	...	...	...

From Fig. 7 we see that kinetic energy is produced in excess of that expected from $K_b(R_{ref})$. This is most likely due to the initial shell of fluid produced by the droplet when it is released from rest. Unlike an expanding bubble which grows to a large size from a macroscopic one, a droplet shrinks from a large size until it evaporates. The effect of the initial conditions is therefore emphasized in the droplet simulations. We see that K_d decreases initially as the droplet shrinks, before rebounding when the fluid shell hits the origin. After this, K_d slowly decreases until the droplet evaporates. It is worth noting that if we used the similarity solution as an initial condition for the fluid profile, then K_d would simply tend toward zero as the droplet would shrink, since the fluid shell size of the similarity solution is relative to the radius of the droplet.

However, it is not clear if a similarity solution would be reached for a realistic three-dimensional simulation, where the initial droplet is nonspherical and the initial velocity field is nonzero. Furthermore, we need to know the final wall velocity for a given η corresponding to the shrinking

similarity solution in order to generate appropriate initial conditions. Currently, this requires running a simulation in any case, making the simulation of the true shrinking similarity solution an iterative process.

Measuring the values for $K_d/K_b(R_{ref})$ at evaporation, we compare these to equivalent values from 3D multibubble simulations. For the multibubble simulations, we plot the maximum value of K [see Eq. (25)] from the simulation, and normalise to $K_b(R_{ref})$ with $R_{ref} = R_*/2$ and R_* the mean bubble separation in the simulation. The resulting plot is shown in Fig. 9. We note that $K/K_b(R_{ref})$ is consistently larger for the spherical droplet simulations than in the 3D multibubble simulations. However, there is a consistent downward trend in both sets of simulations as α is increased, with the exception of $\alpha = 0.005$ for the spherical droplets. Looking at the bottom panel of Fig. 7, we note that the initial value of K_d is significantly larger than $K_b(R_{ref})$, with the value for $\alpha = 0.005$ noticeably smaller. This indicates that we cannot fairly compare our current droplet results to the multibubble results because much more kinetic energy is produced from the initial condition in the droplet case. On the other hand, as explained above, if we did use the similarity solution as an initial condition, the final K_d from a droplet would be close to zero. An accurate estimation of the kinetic efficiency for droplets formed in a multibubble simulation using spherical droplet simulations is therefore unlikely, regardless of the initial conditions used.

A. Self-similar droplets

In this section we explore whether any of the droplets in our simulations reach a similarity solution before evaporating. We qualitatively discuss the process by which a similarity solution forms and its implications for multibubble simulations.

To begin with, we consider the droplet simulation with $\alpha = 0.34$. This appeared to display signs of approaching a similarity solution in the rightmost column of Fig. 6. We first need to reconstruct $\xi = r/\mathcal{T}$, where $\mathcal{T}$ is defined such that $\mathcal{T}T_c = 0$ corresponds to the evaporation of the droplet (see the detailed discussion in Sec. III A). To compare the result of our simulation with the similarity profile, we take $\mathcal{T} = R_d(t)/v_w(t)$, where v_w is negative for a contracting droplet. The velocity and enthalpy profiles in the simulation at late times are plotted as a function of ξ in Fig. 10. We also plot the similarity curves found by integrating Eqs. (21)–(23) starting from $\xi = v_w$ and with the initial velocity (enthalpy) taken from the maximum (minimum) of the corresponding simulation profile. The predicted enthalpy for the similarity solution inside the droplet can be found from Eq. (19). From Fig. 10 we can see that there

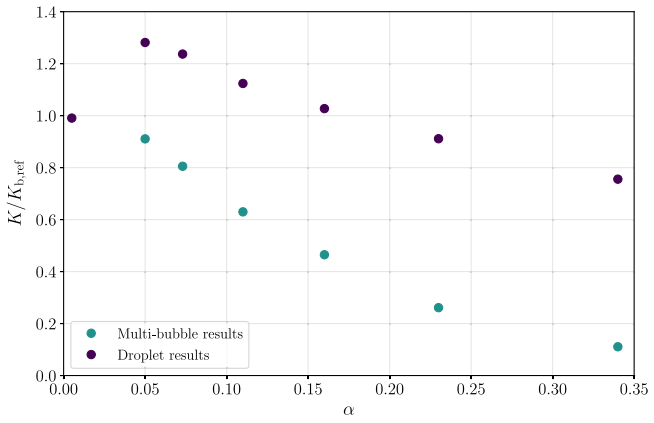

FIG. 9. Comparison of the relative kinetic efficiency $K/K_b(R_{ref})$ in the spherically symmetric 1D droplet simulations and the 3D multibubble simulations of Ref. [46]. The values of $K/K_b(R_{ref})$ are taken from Table IV, see the caption for details.

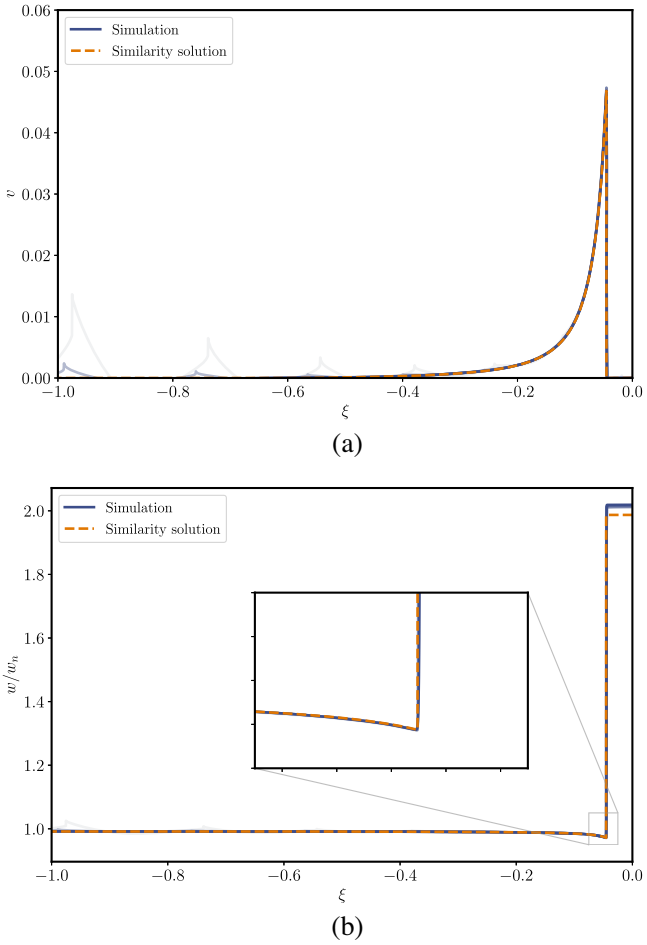

FIG. 10. Comparison between the late-time fluid profile in one of our spherical simulations and a self-similar profile. The upper plot (a) shows the fluid velocity, while the lower plot (b) gives the enthalpy w normalised to the symmetric phase enthalpy at nucleation temperature $w_n \equiv w(0, T_n)$. The simulation shown here in blue has $\alpha = 0.34$. Six equally spaced snapshots of the simulation between $tT_c = 192000$ and $tT_c = 320000$ are shown in blue, with later snapshots shown using darker shades. The self-similarity variable $\xi = r/\mathcal{T}$, where in this case $\mathcal{T} = R_d(t)/v_{w,late}$ with $v_{w,late} = -0.0452$. The dashed line corresponds to the similarity solution obtained by matching v and w against the last timestep shown.

is good agreement at late times for the droplet simulation with $\alpha = 0.34$ and a similarity solution.

A self-similar solution has the fluid at rest inside the droplet.[5] Therefore, for a droplet to become self-similar, the fluid perturbations arising from the inward-propagating shell created by the initial conditions must first exit the droplet. Where we observe this to occur, the process takes place over multiple collisions of the fluid perturbations with the phase boundary and the origin. In each collision with the phase boundary, part of the fluid perturbation is transmitted to the exterior of the droplet. Sufficient time is therefore required for the fluid perturbations to make multiple repeat journeys between the phase boundary and the origin before the droplet evaporates.

As can be seen from Fig. 7, stronger phase transitions cause the phase boundary to propagate at a reduced speed, effectively delaying the evaporation of the droplet and allowing the interior of the droplet to settle to a constant temperature, with the fluid at rest. It is not clear if self-similar solutions would be obtained for the weaker transitions we consider if R_{d0} were to be increased; we leave this for future study.

VI. CONCLUSIONS

In this work, we studied the collapse of spherically symmetric droplets in the coupled field–fluid model with a baglike equation of state. We found the value of η that corresponded to an asymptotic expanding-bubble wall speed of $\xi_{\mathrm{w}} = 0.24$ for a range of transition strengths. This value of η was then used to perform a collapsing droplet simulation.

Our initial conditions consisted of an at-rest tanh-like profile for the scalar field, with the fluid at rest and at the nucleation temperature everywhere. Upon release, an inward-moving fluid shell develops in front of the phase boundary. The fluid shell rebounds upon collision with the origin or with the phase boundary, which can happen multiple times. During a collision with a fluid shell, the phase boundary is decelerated and can even temporarily reverse direction. This effect is more pronounced at higher transition strengths.

The late-time wall velocity for these spherically symmetric droplets approximately agrees with the late-time wall speed found in the multibubble simulations, despite the droplets of Ref. [46] not being spherical. This possibly indicates that the wall velocity is determined by the local conditions across the phase boundary, rather than the large-scale geometry of the droplet itself. On the other hand, the kinetic energy efficiency in the droplets does not match that extracted from multibubble simulations, although the same downward trend in the kinetic efficiency as α increases is observed in both cases. The discrepancy between the simulations is presumably caused by a burst of kinetic energy associated with the generation of the initial fluid shell in the spherical droplet case.

For the strongest transitions, the droplet approaches a self-similarity solution at late times, whereas for our weak and intermediate transitions this does not occur. The approach to a self-similarity solution requires the fluid perturbations to first exit the droplet. In our simulations, this only occurs for strong transitions in which the phase boundary slows significantly. This allows for repeated collisions of the fluid perturbations with the phase boundary and for the perturbations to eventually leave the droplet. Despite this, it appears that the late-time wall velocity found in droplets is more generic than one might expect, as the wall speed in the spherical simulations seem to approximately match the multibubble simulations regardless of whether a self-similar solution develops.

In the case of the strongest transition we considered, the magnitude of the droplet wall velocity drops to less than 10% of that of an isolated expanding bubble with the same value of η. This could modify baryogenesis predictions for strong transitions, as the baryon asymmetry that is generated during a phase transition is strongly dependent on the wall velocity (see Refs. [27–31] for recent results on this phenomenon).

While the kinetic energy efficiency disagrees between the spherical droplet and multibubble simulations, in both cases we saw a decrease in $K/K_{\mathrm{b}}(R_{\mathrm{ref}})$ as α increased. For a self-similarity solution, K_{d} tends toward zero as the droplet shrinks. From the spherical simulations, we saw that stronger transitions have longer to relax toward a similarity solution due to the deceleration of the phase boundary. It is possible that this is also occurring in the multibubble simulations, and that we are seeing the same effect obscured by the fluid perturbations induced by the different initial conditions.

An interesting question is whether a self-similarity solution would eventually develop for a droplet that is produced in a multibubble collision. It seems unlikely that this would occur, as not only are the initial droplets nonspherical, but also in a realistic phase transition there are long-lasting fluid perturbations that propagate in all directions. These fluid perturbations would prevent the interior of the droplet from completely relaxing, which in turn prevents the similarity solution from fully developing.

Our results indicate that important phase transition quantities such as the late-time wall speed can be computed from spherical simulations, reducing the need for expensive 3D multibubble simulations. Other quantities, like the kinetic energy production, are harder to match onto multibubble simulations. One quantity we have not discussed in this work is the fraction of the universe in which droplets are formed. If this fraction could also be estimated using spherical simulations, it could be used in conjunction with the late-time wall speed to provide an estimate for the enhancement factor for the baryon asymmetry. If the kinetic energy efficiency factor for droplets could also be estimated, then a suppression factor for gravitational wave production could be determined using spherical simulations.

[5]Fluid moving inside the droplet would impose a length scale, breaking the self-similarity; it would also have to fit into an ever smaller space as the droplet collapses and $\mathcal{T}T_{\mathrm{c}} \to 0^{-}$.

ACKNOWLEDGMENTS

We acknowledge useful discussions with Mark Hindmarsh, Asier Lopez-Eiguren and Kari Rummukainen, and thank Oliver Gould for helpful comments on an earlier version of this manuscript. D. C. was supported by Academy of Finland Grants No. 328958 and No. 345070. E. V. was supported by the Research Funds of the University of Helsinki and Academy of Finland Grant No. 328958. D. J. W. was supported by Academy of Finland Grants No. 324882 and No. 328958. The authors would also like to thank Finnish Grid and Cloud Infrastructure at the University of Helsinki (urn:nbn:fi:research-infras-2016072533) and CSC—IT Center for Science, Finland, for computational resources. We acknowledge PRACE for awarding us access to HAWK at GCS@HLRS, Germany.

APPENDIX A: WALL SPEED ESTIMATORS

The wall speed can be a challenging quantity to estimate. For isolated droplets and bubbles in our the spherical simulations, the wall speed can be calculated directly from the position of the phase boundary. However, the situation becomes more complicated for 3D multibubble simulations.

In the spherical simulations, we find the wall velocity by tracking the midpoint of the phase boundary. Throughout the simulation we regularly find the position R for which $\phi(R) = \phi_b/2$. The wall velocity v_w is then found via a the time derivative of R using a first-order forward difference

$$v_w(t) \approx \frac{R(t + N\Delta t) - R(t)}{N\Delta t}, \tag{A1}$$

where N refers to the number of timesteps between successive outputs of the position R.

To find an approximate measure of the wall speed $|v_w|$ in the 3D multibubble simulations of Ref. [46], we use two different methods. The first approach is to measure the rate of change of the volume in the broken phase and the area of the phase boundary. On the lattice we approximate the volume in the broken phase to be

$$\mathcal{V}_{\text{broken}} = (\Delta x)^3 \sum_{\mathbf{n}} \begin{cases} 1 & \text{if } \phi_{\mathbf{n}} \geq \phi_b/2, \\ 0 & \text{otherwise.} \end{cases} \tag{A2}$$

where $\mathbf{n}$ denotes the lattice coordinate vector and the summation is over the whole lattice. To find the surface area of the phase boundary we use

$$A = \frac{2}{3}(\Delta x)^2 \sum_{\mathbf{n}}^{N} [f(\phi_{\mathbf{n}}, \phi_{\mathbf{n}+\hat{\imath}}) + f(\phi_{\mathbf{n}}, \phi_{\mathbf{n}+\hat{\jmath}}) + f(\phi_{\mathbf{n}}, \phi_{\mathbf{n}+\hat{k}})], \tag{A3}$$

where the function

$$f(\phi, \phi') = \begin{cases} 1 & \text{if } (\phi - \phi_b/2)(\phi' - \phi_b/2) < 0, \\ 0 & \text{otherwise.} \end{cases} \tag{A4}$$

checks whether the field crosses ϕ_b between two sites. The factor of $2/3$ compensates for the over counting of a the surface area of a sphere represented on a cubic grid in the asymptotic limit of infinitesimally small grid spacing [89]. The average wall speed $|v_w|$ can then be approximated by

$$|v_w| \approx \frac{1}{A} \frac{d\mathcal{V}_{\text{broken}}}{dt}. \tag{A5}$$

We can alternatively compute the wall speed from the kinetic and gradient energies in the scalar field. Assuming that at the phase boundary the scalar field obeys a transport equation

$$\partial_t \phi - \mathbf{v}_w \cdot \nabla \phi = 0, \tag{A6}$$

the average wall speed can then be estimated using

$$|v_w| \approx \sqrt{\frac{E_K}{E_D}}, \tag{A7}$$

where E_K and E_D are the average kinetic and gradient energy densities in the simulation, respectively. We have made use of the fact that the scalar field varies only at the phase boundary.

We compare these two methods in Fig. 11. Both velocity estimators agree for the majority of the duration of all the simulations. The largest disagreement is at late times for the simulation with $\alpha = 0.34$, but even here the estimator from

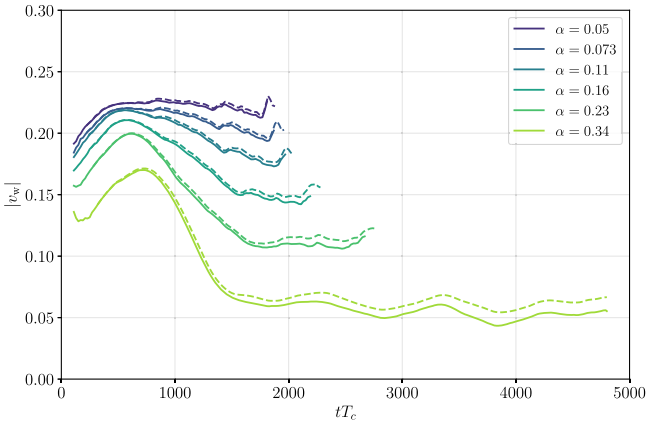

FIG. 11. Comparison of the two different wall speed estimators discussed in this appendix (cf. Fig. 2). The solid line corresponds to the wall speed as estimated using the broken phase volume and phase boundary surface area [cf. Eq. (A5)], whereas the dashed line gives the speed as estimated using the kinetic and gradient energies [cf. Eq. (A7)].

the kinetic and gradient energies differs by at most 20% from the estimator using the broken phase volume and boundary surface area. We use the broken phase volume and boundary surface area estimator in the main body of this paper.

APPENDIX B: EFFECT OF VARYING THE FRACTIONAL CHANGE IN THE DEGREES OF FREEDOM

In the main body of this paper, we focus on a particular choice of the change in the number of light degrees of

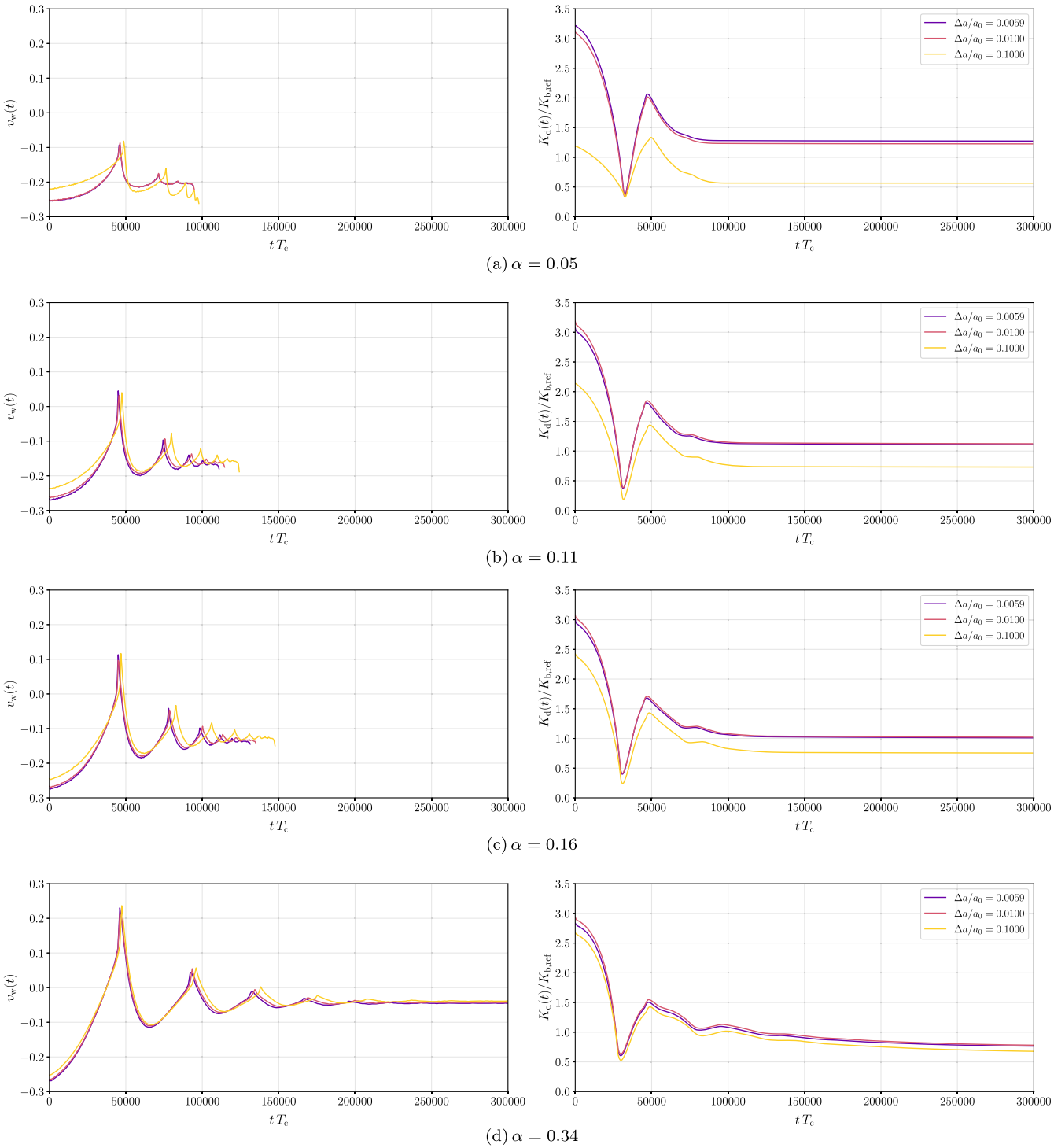

(a) $\alpha = 0.05$

(b) $\alpha = 0.11$

(c) $\alpha = 0.16$

(d) $\alpha = 0.34$

FIG. 12. Plots showing the effect of varying the fractional change in degrees of freedom, $\Delta a/a_0$ on the wall velocity v_w and normalized kinetic energy fraction $K_d/K_b(R_{ref})$. Four choices of α are shown, with the same three choices of $\Delta a/a_0$ shown for each. To allow comparison, the axes are the same for all choices of α; the $\alpha = 0.34$ case is therefore cut off at $t = 300000/T_c$, before the droplets evaporate. As α is increased, the effect of varying $\Delta a/a_0$ becomes milder.

freedom $\Delta a/a_0 \approx 0.0059$. One might expect that stronger transitions are easier to achieve with larger changes in the number of light degrees of freedom; for example, they will in general require less supercooling to achieve a comparable transition strength. It is therefore worth exploring the extent to which the results we present in the main body of this paper depend on our choice of $\Delta a/a_0$.

In Fig. 12 we plot the wall velocity and $K_{\rm d}/K_{\rm b}(R_{\rm ref})$ as a function of time for several phase transition strengths α, for a variety of choices of the fractional change in the number of degrees of freedom across the transition, including $\Delta a/a \approx 0.0059$ used in the main body of the paper.

In varying $\Delta a/a$, we keep M^2 and $l_{\rm w}$ constant. We allow μ and λ to change and then adjust $T_{\rm n}$ and η to achieve the desired α and $\xi_{\rm w}$.

For large α we see good agreement between the different choices of $\Delta a/a_0$ for the observables of interest. Therefore, for strong transitions, the droplet behavior we see in the main body of the paper is expected to occur, independent of the choice of $\Delta a/a_0$.

For smaller α there is some disagreement, with larger changes in the number of degrees of freedom beginning with a shift in the amount of kinetic energy generated at early times. We note that, with our equation of state, the pressure difference across the wall at $T_{\rm n}$ is

$$\begin{aligned}\Delta p &\equiv p(T_{\rm n}, 0) - p(T_{\rm n}, \phi_{\rm b}) \\ &= -\frac{\Delta a}{a_0}\left(1 - \frac{\Delta a}{a_0}\frac{1}{3\alpha}\right) a_0 T_c^4. \end{aligned} \tag{B1}$$

The magnitude of the pressure difference is approximately linear in $\Delta a/a_0$ for sufficiently large α, but it decreases for $\Delta a/a_0 > 3\alpha/2$.

The initial pressure difference determines the initial wall velocity—even though we have adjusted η so that an expanding bubble would reach the same asymptotic wall velocity $\xi_{\rm w}$. A slower initial wall velocity leads to less kinetic energy transfer, which has long-lasting consequences for $K_{\rm d}/K_{\rm b}(R_{\rm ref})$. We believe that this explains the results for $\Delta a/a_0 \gtrsim \alpha$ seen in Fig. 12.

APPENDIX C: CONVERGENCE WITH INITIAL DROPLET RADIUS

In Fig. 13 we show how the wall velocity and $K_{\rm d}/K_{\rm b}(R_{\rm ref})$ vary with time for a variety of different initial droplet radii $R_{\rm d0}$. We normalise the time by the initial radius, and find that for initial radii over one order of magnitude the results collapse onto a single line. Note that the reference radius taken for $K_{\rm b}(R_{\rm ref})$ is, in line with the choice made in Sec. V, the initial droplet radius $R_{\rm d0}$ and hence is different for each case shown.

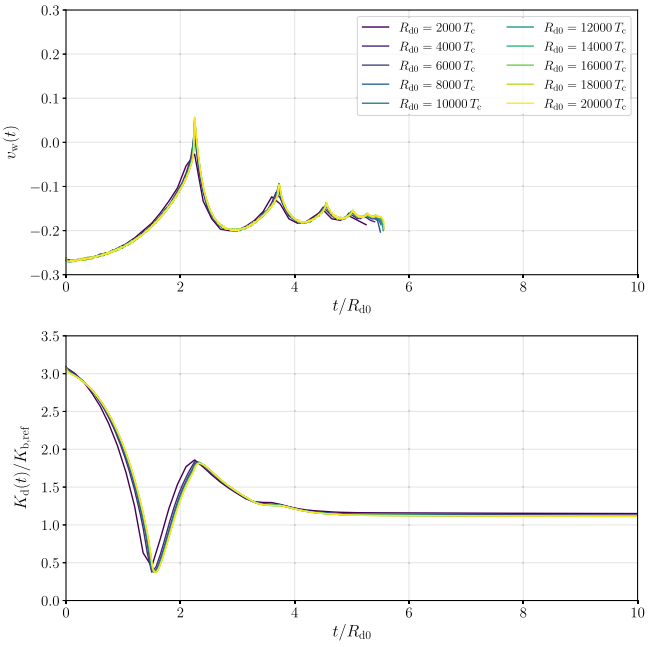

FIG. 13. Plot showing the effect of the initial droplet radius on the results of interest in the main body of the paper, with $\alpha = 0.11$. The wall velocity $v_{\rm w}$ and droplet radius $K_{\rm d}$ normalized to the initial bubble radius $K_{\rm b}(R_{\rm ref})$ are both shown, as a function of time normalized to initial droplet radius $R_{\rm d0}$. The curves generally collapse onto a single line, showing minimal dependence on the initial droplet radius. As in Fig. 7, the lines in the upper plot end when the phase boundary reaches the origin. The measurement interval was kept constant at 1500 timesteps, leading to some aliasing in the results.

The only meaningful combination of length scales in the initial conditions is the bubble wall width relative to the initial radius. In the early universe, the wall width will likely be many orders of magnitude smaller than the radius of a hot droplet, given the difference in scale between the bubble wall width $l_{\rm w}$ and the typical distance between bubbles R_*. The collapse of these curves onto a single line gives us confidence that our results can be extrapolated to the physical case, where the separation is potentially much larger.

[1] A. Mazumdar and G. White, Rep. Prog. Phys. **82**, 076901 (2019).
[2] M. B. Hindmarsh, M. Lüben, J. Lumma, and M. Pauly, SciPost Phys. Lect. Notes **24**, 1 (2021).
[3] D. E. Morrissey and M. J. Ramsey-Musolf, New J. Phys. **14**, 125003 (2012).
[4] D. J. Weir, Phil. Trans. R. Soc. A **376**, 20170126 (2018).
[5] C. Caprini *et al.*, J. Cosmol. Astropart. Phys. 03 (2020) 024.
[6] R. Durrer and A. Neronov, Astron. Astrophys. Rev. **21**, 62 (2013).
[7] T. Vachaspati, Rep. Prog. Phys. **84**, 074901 (2021).
[8] D. Bodeker and G. D. Moore, J. Cosmol. Astropart. Phys. 05 (2017) 025.
[9] S. Höche, J. Kozaczuk, A. J. Long, J. Turner, and Y. Wang, J. Cosmol. Astropart. Phys. 03 (2021) 009.
[10] A. Azatov and M. Vanvlasselaer, J. Cosmol. Astropart. Phys. 01 (2021) 058.
[11] B. Laurent and J. M. Cline, Phys. Rev. D **102**, 063516 (2020).
[12] Y. Bea, J. Casalderrey-Solana, T. Giannakopoulos, D. Mateos, M. Sanchez-Garitaonandia, and M. Zilhão, Phys. Rev. D **104**, L121903 (2021).
[13] Y. Gouttenoire, R. Jinno, and F. Sala, J. High Energy Phys. 05 (2022) 004.
[14] G. C. Dorsch, S. J. Huber, and T. Konstandin, J. Cosmol. Astropart. Phys. 04 (2022) 010.
[15] S. De Curtis, L. D. Rose, A. Guiggiani, A. G. Muyor, and G. Panico, J. High Energy Phys. 03 (2022) 163.
[16] Y. Bea, J. Casalderrey-Solana, T. Giannakopoulos, A. Jansen, D. Mateos, M. Sanchez-Garitaonandia, and M. Zilhão, J. High Energy Phys. 09 (2022) 008.
[17] O. Gould, J. Kozaczuk, L. Niemi, M. J. Ramsey-Musolf, T. V. I. Tenkanen, and D. J. Weir, Phys. Rev. D **100**, 115024 (2019).
[18] K. Kainulainen, V. Keus, L. Niemi, K. Rummukainen, T. V. I. Tenkanen, and V. Vaskonen, J. High Energy Phys. 06 (2019) 075.
[19] D. Croon, O. Gould, P. Schicho, T. V. I. Tenkanen, and G. White, J. High Energy Phys. 04 (2021) 055.
[20] O. Gould and J. Hirvonen, Phys. Rev. D **104**, 096015 (2021).
[21] D. Croon, E. Hall, and H. Murayama, arXiv:2104.10687.
[22] O. Gould and T. V. I. Tenkanen, J. High Energy Phys. 06 (2021) 069.
[23] J. Hirvonen, J. Löfgren, M. J. Ramsey-Musolf, P. Schicho, and T. V. I. Tenkanen, J. High Energy Phys. 07 (2022) 135.
[24] J. Löfgren, M. J. Ramsey-Musolf, P. Schicho, and T. V. I. Tenkanen, arXiv:2112.05472.
[25] A. Ekstedt, Eur. Phys. J. C **82**, 173 (2022).
[26] A. Ekstedt, J. High Energy Phys. 08 (2022) 115.
[27] J. M. Cline and K. Kainulainen, Phys. Rev. D **101**, 063525 (2020).
[28] A. Azatov, M. Vanvlasselaer, and W. Yin, J. High Energy Phys. 10 (2021) 043.
[29] I. Baldes, S. Blasi, A. Mariotti, A. Sevrin, and K. Turbang, Phys. Rev. D **104**, 115029 (2021).
[30] G. C. Dorsch, S. J. Huber, and T. Konstandin, J. Cosmol. Astropart. Phys. 08 (2021) 020.
[31] M. Lewicki, M. Merchand, and M. Zych, J. High Energy Phys. 02 (2022) 017.
[32] F. R. Ares, M. Hindmarsh, C. Hoyos, and N. Jokela, J. High Energy Phys. 04 (2021) 100.
[33] F. Bigazzi, A. Caddeo, A. L. Cotrone, and A. Paredes, J. High Energy Phys. 12 (**2020**) 200.
[34] Y. Bea, J. Casalderrey-Solana, T. Giannakopoulos, A. Jansen, S. Krippendorf, D. Mateos, M. Sanchez-Garitaonandia, and M. Zilhão, arXiv:2112.15478.
[35] F. R. Ares, O. Henriksson, M. Hindmarsh, C. Hoyos, and N. Jokela, Phys. Rev. D **105**, 066020 (2022).
[36] C. Gowling and M. Hindmarsh, J. Cosmol. Astropart. Phys. 10 (2021) 039.
[37] F. Giese, T. Konstandin, and J. van de Vis, J. Cosmol. Astropart. Phys. 11 (2021) 002.
[38] R. Jinno, T. Konstandin, and H. Rubira, J. Cosmol. Astropart. Phys. 04 (2021) 014.
[39] R. Jinno, T. Konstandin, H. Rubira, and J. van de Vis, J. Cosmol. Astropart. Phys. 12 (**2021**) 019.
[40] A. Roper Pol, S. Mandal, A. Brandenburg, T. Kahniashvili, and A. Kosowsky, Phys. Rev. D **102**, 083512 (2020).
[41] T. Kahniashvili, A. Brandenburg, G. Gogoberidze, S. Mandal, and A. Roper Pol, Phys. Rev. Res. **3**, 013193 (2021).
[42] A. Roper Pol, S. Mandal, A. Brandenburg, and T. Kahniashvili, J. Cosmol. Astropart. Phys. 04 (2022) 019.
[43] A. Brandenburg, G. Gogoberidze, T. Kahniashvili, S. Mandal, A. Roper Pol, and N. Shenoy, Classical Quantum Gravity **38**, 145002 (2021).
[44] J. Dahl, M. Hindmarsh, K. Rummukainen, and D. Weir, Phys. Rev. D **106**, 063511 (2022).
[45] A. Roper Pol, C. Caprini, A. Neronov, and D. Semikoz, Phys. Rev. D **105**, 123502 (2022).
[46] D. Cutting, M. Hindmarsh, and D. J. Weir, Phys. Rev. Lett. **125**, 021302 (2020).
[47] R. Jinno, H. Seong, M. Takimoto, and C. M. Um, J. Cosmol. Astropart. Phys. 10 (2019) 033.
[48] D. Cutting, M. Hindmarsh, and D. J. Weir, Phys. Rev. D **97**, 123513 (2018).
[49] D. Cutting, E. G. Escartin, M. Hindmarsh, and D. J. Weir, Phys. Rev. D **103**, 023531 (2021).
[50] M. Lewicki and V. Vaskonen, Eur. Phys. J. C **80**, 1003 (2020).
[51] M. Lewicki and V. Vaskonen, Eur. Phys. J. C **81**, 437 (2021).
[52] M. Lewicki, O. Pujolàs, and V. Vaskonen, Eur. Phys. J. C **81**, 857 (2021).
[53] O. Gould, S. Sukuvaara, and D. Weir, Phys. Rev. D **104**, 075039 (2021).
[54] E. Witten, Phys. Rev. D **30**, 272 (1984).
[55] C. Alcock and E. Farhi, Phys. Rev. D **32**, 1273 (1985).
[56] K. Kajantie and H. Kurki-Suonio, Phys. Rev. D **34**, 1719 (1986).
[57] C. Alcock and A. Olinto, Phys. Rev. D **39**, 1233 (1989).
[58] H. Kurki-Suonio, Phys. Rev. D **37**, 2104 (1988).
[59] M. L. Olesen and J. Madsen, Phys. Rev. D **43**, 1069 (1991); **44**, 566(E) (1991).
[60] J. Ignatius, K. Kajantie, H. Kurki-Suonio, and M. Laine, Phys. Rev. D **49**, 3854 (1994).
[61] A. F. Heckler, Phys. Rev. D **51**, 405 (1995).
[62] M. Hindmarsh, Phys. Rev. D **45**, 1130 (1992).
[63] A. R. Zhitnitsky, J. Cosmol. Astropart. Phys. 10 (2003) 010.

[64] S. Ge, K. Lawson, and A. Zhitnitsky, Phys. Rev. D **99**, 116017 (2019).
[65] A. Zhitnitsky, Mod. Phys. Lett. A **36**, 2130017 (2021).
[66] Y. Bai, A. J. Long, and S. Lu, Phys. Rev. D **99**, 055047 (2019).
[67] L. Rezzolla, J. Miller, and O. Pantano, Phys. Rev. D **52**, 3202 (1995).
[68] L. Rezzolla and J. C. Miller, Phys. Rev. D **53**, 5411 (1996).
[69] H. Kurki-Suonio and M. Laine, Phys. Rev. D **54**, 7163 (1996).
[70] H. Kurki-Suonio and M. Laine, Phys. Rev. Lett. **77**, 3951 (1996).
[71] K. Enqvist, J. Ignatius, K. Kajantie, and K. Rummukainen, Phys. Rev. D **45**, 3415 (1992).
[72] P. John and M. G. Schmidt, Nucl. Phys. **B598**, 291 (2001); **B648**, 449(E) (2003).
[73] T. Konstandin, G. Nardini, and I. Rues, J. Cosmol. Astropart. Phys. 09 (2014) 028.
[74] G. C. Dorsch, S. J. Huber, and T. Konstandin, J. Cosmol. Astropart. Phys. 12 (2018) 034.
[75] J. M. Cline, A. Friedlander, D.-M. He, K. Kainulainen, B. Laurent, and D. Tucker-Smith, Phys. Rev. D **103**, 123529 (2021).
[76] P. J. Steinhardt, Phys. Rev. D **25**, 2074 (1982).
[77] H. Kurki-Suonio, Nucl. Phys. **B255**, 231 (1985).
[78] J. R. Espinosa, T. Konstandin, J. M. No, and G. Servant, J. Cosmol. Astropart. Phys. 06 (**2010**) 028.
[79] M. Hindmarsh and M. Hijazi, J. Cosmol. Astropart. Phys. 12 (2019) 062.
[80] L. Rezzolla and O. Zanotti, *Relativistic Hydrodynamics*, EBSCO ebook academic collection (OUP, Oxford, 2013).
[81] M. Hindmarsh, S. J. Huber, K. Rummukainen, and D. J. Weir, Phys. Rev. D **92**, 123009 (2015).
[82] M. Hindmarsh, S. J. Huber, K. Rummukainen, and D. J. Weir, Phys. Rev. D **96**, 103520 (2017).
[83] J. Centrella and J. R. Wilson, Astrophys. J. **273**, 428 (1983).
[84] J. Centrella and J. R. Wilson, Astrophys. J. Suppl. Ser. **54**, 229 (1984).
[85] H. Kurki-Suonio, R. A. Matzner, J. Centrella, and J. R. Wilson, Phys. Rev. D **35**, 435 (1987).
[86] J. Crank and P. Nicolson, Math. Proc. Cambridge Philos. Soc. **43**, 50 (1947).
[87] D. Cutting (2019), see movies of strong phase transitions available at https://vimeo.com/album/5968055.
[88] D. Cutting, E. Vilhonen, and D. J. Weir, Droplet collapse during strongly supercooled transitions: Movies of collapsing droplets, Movie on Zenodo, 10.5281/zenodo.6390336 (2022).
[89] H. Pfoertner, Entry A085690 in The On-Line Encyclopedia of Integer Sequences (2003).